Sparse Reconstruction for Near-Field MIMO Radar Imaging Using Fast Multipole Method

EMRE A. MIRAN[ID]**, FIGEN S. OKTEM**[ID]**, (Member, IEEE), AND SENCER KOC**
Electrical and Electronics Engineering Department, Middle East Technical University, 06800 Ankara, Turkey

Corresponding author: Emre A. Miran (alpmiran@gmail.com)

ABSTRACT Radar imaging using multiple input multiple output systems are becoming popular recently. These applications typically contain a sparse scene and the imaging system is challenged by the requirement of high quality real-time image reconstruction from under-sampled measurements via compressive sensing. In this paper, we deal with obtaining sparse solution to near- field radar imaging problems by developing efficient sparse reconstruction, which avoid storing and using large-scale sensing matrices. We demonstrate that the ''fast multipole method'' can be employed within sparse reconstruction algorithms to efficiently compute the sensing operator and its adjoint (backward) operator, hence improving the computation speed and memory usage, especially for large-scale 3-D imaging problems. For several near-field imaging scenarios including point scatterers and 2-D/3-D extended targets, the performances of sparse reconstruction algorithms are numerically tested in comparison with a classical solver. Furthermore, effectiveness of the fast multipole method and efficient reconstruction are illustrated in terms of memory requirement and processing time.

INDEX TERMS Multiple-input-multiple-output radar imaging, near-field imaging, inverse problem, sparse reconstruction, fast multipole method.

I. INTRODUCTION

Radar imaging has many applications such as subsurface or behind wall imaging, improvised explosive device detection, and collision avoidance and has been of interest in the literature, recently [1]–[4]. For high resolution imaging systems, planar arrays with a large number of antenna elements is used and the antenna is generally a multiple-input-multiple-output (MIMO) array composed of spatially distributed transmitting and receiving sub-arrays, operating sequentially or simultaneously. In many of these applications the target to be imaged lies in the near field of the antenna array. The spatial diversity of the sub-arrays, in association with wideband operation, provides high resolution and image quality with few number of antennas [5], [6].

A near-field MIMO imaging problem can be numerically modeled as a linear inverse problem whose solution contains the position, shape, and reflectivity distribution of the target. However, the solution is usually not unique due to under-determined nature of the problem. Besides, ill-posed structure

of the linear system makes it difficult to reconstruct high quality images from noisy measurements. In order to generate useful images, additional regularization approaches must be considered [7].

In the last two decades, researchers have developed many regularization methods to overcome shortcomings of the inverse problem and yield improvement at the quality of its solution. One fundamental approach that has been suggested as a regularizer, particularly for compressive sensing (CS)-based imaging settings [8]–[11], [27], [28], [39], is sparsity constraint. The sparsity constraint provides an approximate solution that contains few non-zero entries when compared to its dimension. This approach is also known as sparse approximation [12], [13] and mathematically expressed as

$$\max_{\mathbf{x}} \phi(\mathbf{x}) \quad \text{subject to } \mathbf{Ax} = \mathbf{b} \qquad (1)$$

where ϕ is referred to as regularization (or cost) function. Depending on the choice of ϕ, reconstruction characteristic of the imaged space varies. The most basic approach is to generate a maximally sparse representation by selecting

---

$\phi(\mathbf{x}) = \|\mathbf{x}\|_0$ where $\|.\|_0 : \mathbb{R}^N \to \mathbb{R}$ is ℓ_0 "norm", which gives the number of non-zero entries of a vector in $\mathbb{R}^N$.

Orthogonal matching pursuit (OMP) is a greedy method based on ℓ_0 "norm". It approximates a sparse solution by iteratively selecting a column of the sensing matrix, which contribute to the sparsity most. The iterations are continued until a predetermined sparsity level is reached. Stage-wise orthogonal matching pursuit (StOMP) is another type of greedy method based on OMP. It simply differs from OMP by selecting multiple columns at each iteration, namely stage, which makes it converge faster than OMP. Regularized orthogonal matching pursuit (ROMP) is a modified form of OMP that does not possess a threshold value for sparsity level; instead it selects the columns having similar dot products with the solution vector. Despite the fact that these methods are able to converge in very short runtime, they generally do not offer any guarantee for a sparse solution [14]–[16]. Moreover, the complexity of the search for all possible sparse subsets is generally exponential in the number of columns, which makes the solution of (1) with ℓ_0 "norm" NP-hard [17]. Greedy methods work under specific conditions and does not require exhaustive search.

Another useful approach for sparse approximation is to replace the ℓ_0 "norm" with ℓ_1-norm, which converts the inverse problem into a convex optimization problem. Alternating direction method of multipliers (ADMM) is based on ℓ_1-norm and has been used for various imaging problems [18]–[21]. It is a form of augmented Lagrangian method (ALM), which handles solution of the optimization problem more efficiently by dividing it into smaller components. ADMM splits primal variables, augments the Lagrangian of the optimization problem (as in method of multipliers) and carries out iterative variable minimization steps. There also exist split augmented Lagrangian shrinkage algorithm (SALSA) [21], [22] and constrained-SALSAs (C-SALSA-1/C-SALSA-2) [19]. These techniques transform the unconstrained expression of the problem into a constrained one by performing variable splitting and using an ALM, specifically ADMM.

Tikhonov regularization, which is based on ℓ_2-norm, is a simple tool specialized for regularizing ill-posed problems [23]. Although it regularizes conditioning of problems, it generally does not offer a sparse solution. In [24], two sparse reconstruction algorithms are proposed based on generalized Arnoldi-Tikhonov regularization, approximating ℓ_1-norm and total variation (TV) in terms of ℓ_2-norm. These algorithms can provide a sparse solution for the problem within fewer iterations than classical Tikhonov regularization algorithm at the cost of higher relative error.

All the sparse approximation methods mentioned above attempt to solve the inverse problem through iterative matrix-vector multiplications, which are equivalent to computing the (forward) sensing operator and its (backward) adjoint operator. As the imaging problem gets electrically larger, solution of the forward problem becomes difficult to store and requires immense computational resources with complexities

of $O(IN^2)$ and $O(N^2)$ for processing time and memory, respectively, where N is the number of unknowns and I is the iteration count. In the literature, therefore, much effort has been made, searching for methods to reduce computational complexity of the 3-D imaging problems. For instance, in [25], authors propose an accelerated algorithm based on Bayesian learning and approximate message passing to solve large-scale electrical impedance tomography problem. Commonly, diagonalizability of the sensing operator and fast Fourier transforms are exploited for efficient large-scale sparse reconstruction, for example in optical volumetric imaging [26] and compressive spectral imaging [27]. Similarly, for wideband near-field radar imaging, in [28], efficient CS reconstruction is achieved by decomposing the sensing operator into Fourier transform and sampling operations, and in [29], sensing operator is computed using an interpolation-free holographic imaging algorithm that also involves fast Fourier transforms. These approaches reduce memory usage and computation time for a near-field radar imaging with a *monostatic* configuration.

Here we demonstrate that the "fast multipole method" can be employed within sparse reconstruction algorithms to efficiently compute the sensing operator and its adjoint (backward) operator, for a general *multistatic* imaging setting. The forward part of the radar imaging problem is an electromagnetic scattering problem and the fast multipole method (FMM) is a powerful tool to efficiently calculate the large matrix-vector products for the forward (sensing) operator. In fact, FMM can be used to calculate the matrix-vector product without forming the sensing matrix explicitly and has the ability to decrease the computation time to $O(IN^{3/2})$ and reduce memory requirement to $O(N^{3/2})$ [30]–[33].

In this paper, we seek accelerated sparse solution to near-field multiple-input-multiple-output (MIMO) radar imaging problem. For this purpose, we initially construct the problem as a convex optimization problem with sparsity (ℓ_1-norm and TV regularization) and solve it by using the augmented Lagrangian framework. Then, for large-scale imaging problems, we propose employing the FMM formulation to efficiently compute the matrix-vector multiplications within the reconstruction algorithm. Hence, the novelty of this study is to develop efficient sparsity-based reconstruction methods that exploit FMM formulation for matrix-vector multiplications involved, enabling significant reduction in computation time and memory requirement. Several numerical simulations are carried out for 2D and 3D objects as well as point scatterers in order to validate the study. The effectiveness of the FMM is also demonstrated in terms of memory usage and computation time by comparing it with classical direct and iterative linear system solvers.

This paper is organized as follows. Section II introduces imaging configuration and its representation as a linear system. In section III, application of the FMM to solution of inverse problem is described briefly. Section IV presents mathematical basis of inverse problem. Section V deals with the algorithmic approaches for numerical solution of the
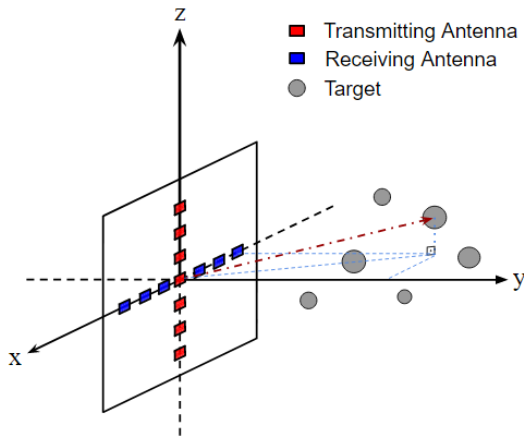
FIGURE 1. A plus-shaped 2-D planar MIMO array.

II. FORWARD PROBLEM
The construction of the forward problem is the key to establish the mathematical relation between the reflectivity distribution of the imaging scene and the measurement data, and hence is essential for the development of the imaging algorithm. The solution of the inverse problem can then be carried out by iterations and this requires solving the forward problem at each iteration step. Therefore, a fast and robust algorithm that computes the forward (sensing) operator is required for efficient and accurate image reconstruction.

In this study, an ultra-wideband (UWB) near field MIMO array imaging structure, as introduced in [34], [35], is considered. We will assume that the data is collected by transmitting sequentially from each element of the transmit array and receiving simultaneously by the receiving array elements of the MIMO array. The imaging structure is depicted in Fig. 1. A two dimensional plus-shaped MIMO array located in $y = 0$ plane is used. The receiving antennas are positioned along the x-axis and their locations are denoted by $(x_R, 0, z_R)$ while the transmitting antennas are placed along the z-axis and their locations are denoted by $(x_T, 0, z_T)$. Despite the vector nature of the scattering phenomenon, we will use a simple scalar model that is commonly used in the literature [36]. Applying the Born approximation, the scattered field at the corresponding receiving antenna position due to any scatterer in the imaging volume (x, y, z) is mathematically expressed as [30], [31]

$$s(x_T, z_T, x_R, z_R, t) = \int\int\int \frac{1}{4\pi R_T R_R} f(x, y, z) p$$
$$\times \left(t - \left[\frac{R_T}{c} + \frac{R_R}{c} \right] \right) dx dy dz \quad (2)$$

where $p(t)$ is the transmitted pulse in time domain, c is speed of light, and $f(x, y, z)$ is the three dimensional

reflectivity distribution function of the target. R_T and R_R denote the distances to the point (x, y, z) from the transmitting and the receiving antennas, respectively, and can be written as

$$R_T = \sqrt{(x_T - x)^2 + y^2 + (z_T - z)^2}, \quad (3)$$
$$R_R = \sqrt{(x_R - x)^2 + y^2 + (z_R - z)^2}. \quad (4)$$

By taking temporal Fourier transform of (2), the received signal can be written in the frequency domain as

$$s(x_T, z_T, x_R, z_R, k) = 4\pi p(k) \int\int\int \frac{e^{-jkR_T}}{4\pi R_T} \frac{e^{-jkR_R}}{4\pi R_R} f$$
$$\times (x, y, z) dx dy dz \quad (5)$$

where $p(k)$ is the Fourier transform of the transmitted pulse with k being the wavenumber.

Considering a computerized image reconstruction process, continuous expressions in (2) and (5) can be discretized by expressing the three dimensional reflectivity distribution function in terms of voxels, thus, (5) can be written as:

$$y_{T_m, R_n, q, k_l} = p(k_l) \sum_{q=1}^{N_V} \frac{e^{-jk_l(R_{T_m,q} + R_{q,R_n})}}{4\pi R_{T_m,q} R_{q,R_n}} f_q \quad (6)$$

where N_V is number of voxels and f_q is reflectivity of the qth voxel. The transmitting antennas radiate N_F discrete frequencies, which are equally spaced by frequency step of Δf, in the operational bandwidth. $R_{T_m,q}$ denotes the distance from the mth transmitting antenna to the center of the qth voxel and R_{q,R_n} denotes the distance from the center of the qth voxel to the nth receiving antenna. Furthermore, the number of transmitting and receiving antennas are N_T and N_R, respectively.

Note that the scattered field expressed in (6) is obtained by ignoring multiple reflections among the voxels. The transmitted pulse is assumed to be directly reflected by each voxel to the corresponding receiving antenna without any contribution from the rest of the voxels.

The discrete model defines a linear system as given in (7). The reflectivity values of the voxels are organized in the vector **f** in a lexicographic order and the measurements are listed in the same order in the right-hand-side vector **y**. The matrix $\mathbf{A} \in \mathbb{C}^{M \times N}$ is the sensing (system) matrix and its total number of rows M, is equal to $N_T \times N_R \times N_F$, whereas the number of columns N, is equal to N_V.

$$\mathbf{Af} = \mathbf{y} \quad (7)$$

The open form of this linear system is given in (8), as shown at the bottom of the next page.

For the solution of such a linear system using an iterative algorithm, $N_T \times N_R \times N_F \times N_V$ multiplications must be performed for one matrix-vector product. This means that as the dimension of the unknown vector increases,
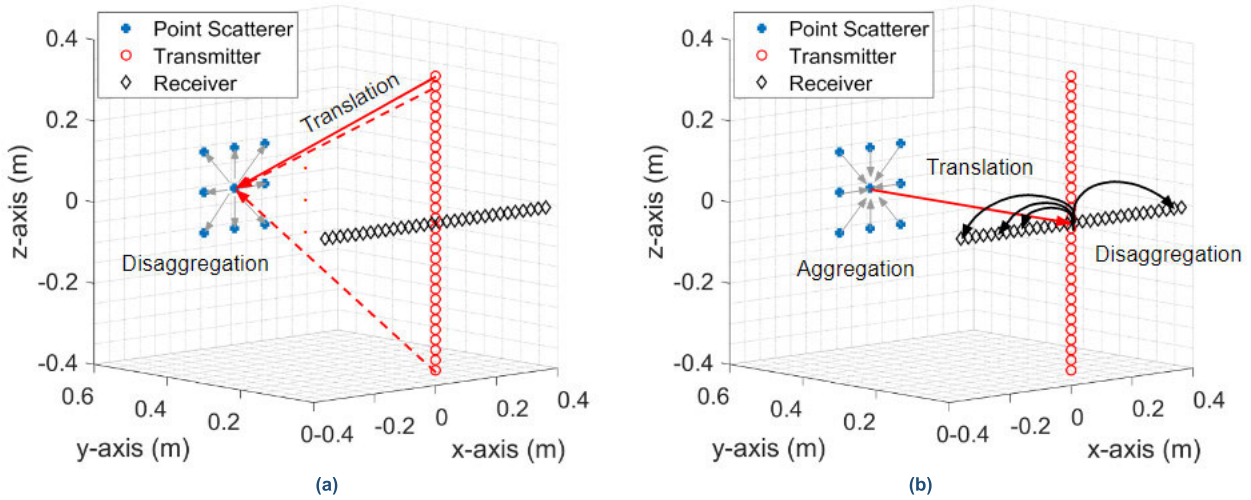
FIGURE 2. Two-stage FMM. (a) 1st stage and (b) 2nd stage.

the solution becomes quite inefficient due to the requirements for excessive amount of computational resources and memory.

III. FAST MULTIPOLE METHOD

In this study, we solve the imaging problem by iterative methods, where each iteration requires the computation of the forward operator (multiplication of a vector with the sensing matrix $\mathbf{A}$) and its adjoint (multiplication of a vector with the matrix $\mathbf{A}^H$). As expressed in (8), entries of the sensing matrix $\mathbf{A}$ are product of two Green's functions, which is the fundamental factor that allows us to use FMM for the solution of the forward problem through a two stage process. The first Green's function represents the path that the transmitted signal travels from the transmitting antenna to the target and

it is treated by the first stage of FMM. The second Green's function represents the propagation of the reflected signal back to the receiving antenna and the second stage of the FMM is applied to this part. Details of both stages are given below.

Note that classical FMM involves three main steps: Aggregation, translation, and disaggregation [30]–[32].

A. THE FIRST STAGE

As depicted in Fig. 2(a), we assume that only one transmitting antenna operates at a time. The aggregation step, therefore, is not applied in this stage. The transmitted signal is directly translated from m^{th} transmitting antenna to the geometric center of the imaging domain and then distributed to each voxel by disaggregation step. This phenomenon is mathematically

$$
4\pi
\begin{bmatrix}
p\left(k_1\right) \dfrac{e^{-jk_1 R_{T_1,1}}}{4\pi R_{T_1,1}} \dfrac{e^{-jk_1 R_{1,R_1}}}{4\pi R_{1,R_1}} & \cdots & \cdots & p\left(k_1\right) \dfrac{e^{-jk_1 R_{T_1,N_V}}}{4\pi R_{T_1,N_V}} \dfrac{e^{-jk_1 R_{N_V,R_1}}}{4\pi R_{N_V,R_1}} \\
\vdots & \vdots & \vdots & \vdots \\
p\left(k_1\right) \dfrac{e^{-jk_1 R_{T_1,1}}}{4\pi R_{T_1,1}} \dfrac{e^{-jk_1 R_{1,R_{N_R}}}}{4\pi R_{1,R_{N_R}}} & \cdots & \cdots & p\left(k_1\right) \dfrac{e^{-jk_1 R_{T_1,N_V}}}{4\pi R_{T_1,N_V}} \dfrac{e^{-jk_1 R_{N_V,R_{N_R}}}}{4\pi R_{N_V,R_{N_R}}} \\
\vdots & \vdots & \vdots & \vdots \\
p\left(k_1\right) \dfrac{e^{-jk_1 R_{T_{N_T},1}}}{4\pi R_{T_{N_T},1}} \dfrac{e^{-jk_1 R_{1,R_{N_V}}}}{4\pi R_{1,R_{N_V}}} & \cdots & \cdots & p\left(k_1\right) \dfrac{e^{-jk_1 R_{T_{N_T},S}}}{4\pi R_{T_{N_T},S}} \dfrac{e^{-jk_1 R_{S,R_{N_R}}}}{4\pi R_{S,R_{N_R}}} \\
\vdots & \vdots & \vdots & \vdots \\
p\left(k_l\right) \dfrac{e^{-jk_l R_{T_{N_T},1}}}{4\pi R_{T_{N_T},1}} \dfrac{e^{-jk_l R_{1,R_{N_V}}}}{4\pi R_{1,R_{N_V}}} & \cdots & \cdots & p\left(k_l\right) \dfrac{e^{-jk_l R_{T_{N_T},S}}}{4\pi R_{T_{N_T},S}} \dfrac{e^{-jk_l R_{S,R_{N_R}}}}{4\pi R_{S,R_{N_R}}}
\end{bmatrix}
\cdot
\begin{bmatrix}
f_1 \\ \vdots \\ \vdots \\ \vdots \\ f_{N_V}
\end{bmatrix}
=
\begin{bmatrix}
y_1 \\ \vdots \\ \vdots \\ \vdots \\ y_M
\end{bmatrix}
\tag{8}
$$

expressed as

$$y_{T_m, q, k_l, FMM} = \int T_{\tau, m}\left(k_l, \hat{\boldsymbol{u}}, \boldsymbol{R}_{Tm}\right) D_q\left(k_l, \hat{\boldsymbol{u}}, r_q\right) f_q d\hat{\boldsymbol{u}}$$

$$(9)$$

where

$$T_{\tau, m}\left(k, \hat{\boldsymbol{u}}, R_{Tm}\right) = \frac{jk}{(4\pi)^2} \sum_{t=0}^{\tau} j^t\left(2t + 1\right) h_t^{(1)}$$
$$\times \left(k\left|\boldsymbol{R}_{Tm}\right|\right) P_t\left(\hat{\boldsymbol{u}} \cdot \hat{R}_{Tm}\right) \quad (10)$$

$$D_q\left(k_l, \hat{\boldsymbol{u}}, r_q\right) = e^{jk_l \hat{\boldsymbol{u}} \cdot r_q} \quad (11)$$

The quantities in (10) and (11) are referred to as the translation function and the disaggregation function, respectively, where τ is the order of truncation for the translation function, $h_t^{(1)}(x)$ is the spherical Hankel function of the first kind and t^{th} order, and $P_t(x)$ is the Legendre polynomial of order t. The excess bandwidth formula (EBF) is used to determine the truncation order [37], [38].

Integration is over a unit sphere and it is implemented numerically by using Gauss-quadrature rule. The sample points for the integration along elevation and azimuth axes are determined by using the truncation order. Note that as many translation functions as the number of transmitting antennas are required at this stage.

The number of operations carried out in this stage is $N_T \times N_V \times N_F$ since (9) must be repeated for each voxel and receiving antenna positions as well as each frequency steps.

B. THE SECOND STAGE

Fig. 2(b) demonstrates that the scattered signals (excluding the multiple reflections) from every voxel of the target is re-collected at geometric center of the image volume in aggregation step. The total signal is then translated back to geometric center of the receiving antennas, and, the received signal is redistributed among the receiving antennas through disaggregation step. Mathematical expression of this stage is given as follows

$$y_{r_q, R_r, r_n, k_l, FMM} = \int A_q\left(k_l, \hat{\boldsymbol{u}}, r_q\right) T_\tau\left(k_l, \hat{\boldsymbol{u}}, R_r\right)$$
$$\times D_n\left(k_l, \hat{\boldsymbol{u}}, r_n\right) f_q d\hat{\boldsymbol{u}} \quad (12)$$

where

$$A_q\left(k_l, \hat{\boldsymbol{u}}, r_n\right) = e^{jk_l \hat{\boldsymbol{u}} \cdot r_n} \quad (13)$$

is the aggregation function, R_r is the distance from the center of the image volume to the geometric center of the receiving antennas, r_q is the distance from q^{th} voxel to the center of the image volume, and r_n is the distance from geometric center of the receiving antennas to the nth receiving antenna. This stage lasts shorter than the first stage since it contains only one translation. Note that (12) must be repeated for each voxel position, receiving antenna position and frequency steps. Hence, the total number of operations required in this stage is $N_V \times N_R \times N_F$.

The above explanations describe how the forward (sensing) operator is computed using FMM formulation. The same procedure can also be applied for the computation of the adjoint (backward) operator by simply exchanging order of the stages, i.e., in the 1st stage, aggregation, translation and disaggregation operations are carried out, while translation and disaggregation operations are performed in the 2nd stage.

Consequently, FMM reduces the overall operations needed for the evaluation of a single matrix-vector product to $(N_T + N_R) \times N_V \times N_F$ as compared to classical direct muliplication, which requires $N_T \times N_R \times N_V \times N_F$ operations. This reduction leads to an efficient solution in terms of processing time and memory for the solution of imaging problems where relatively large antenna arrays are used.

IV. INVERSE PROBLEM

This section deals with estimation of reflectivity distribution of the imaged scene from measurements using the MIMO array. The reflectivity of a physical object is generally a smooth function and its values at neighboring points are highly correlated along down- and cross-range directions, which allows it to be represented in a sparse form when an appropriate regularization function $\phi(\mathbf{f})$ is introduced [40]. The sparsity-inducing regularization problem is formulated in unconstrained form as

$$\min_{\mathbf{f}} \frac{1}{2} \|\mathbf{Af} - \mathbf{y}\|_2^2 + \lambda\phi(\mathbf{f}) \quad (14)$$

where $\lambda > 0$ is regularization parameter, which controls the sparsity and determines the trade-off between the regularization and data fidelity [14]. In particular, λ should be increased as signal-to-noise ratio (SNR) decreases. An alternative form is the constrained problem of

$$\min_{\mathbf{f}} \phi(\mathbf{f}) \quad \text{subject to} \quad \|\mathbf{Af} - \mathbf{y}\|_2 \le \varepsilon \quad (15)$$

where ε is error tolerance, which is introduced when the measurement data is noisy and its value is estimated using SNR of the received signal. In (14) and (15), $\phi(\cdot)$ acts as a transform operator, which can be selected with respect to the physical characteristic of the imaged scene, e.g., it can be selected as ℓ_1-norm ($\|\mathbf{f}\|_1$) for point scatterers with weak background, whereas common choice for two- and three-dimensional extended targets is discrete gradient operator of the following form

$$\phi = \begin{bmatrix} D_x \\ D_y \\ D_z \end{bmatrix} \quad (16)$$

where D_x, D_y, and D_z corresponds to difference operators along x-, y-, and z-axis, respectively. This operation is called total variation (TV) of the unknown and leads to a reconstruction where sharp edges and rapidly changing structures are preserved on the reconstructed image [40]. The mathematical expression of three-dimensional TV is [18]

$$TV\left(|\mathbf{f}|\right) = \sum_{i,j,k} |\nabla\left(|\mathbf{f}|\right)|, \quad (17)$$

$$|\nabla(|\mathbf{f}|)| = \sqrt{D_x(|\mathbf{f}|)^2 + D_y(|\mathbf{f}|)^2 + D_z(|\mathbf{f}|)^2} \quad (18)$$

and

$$
\begin{aligned}
D_x(|\mathbf{f}|) &= |\mathbf{f}[i+1,j,k]| - |\mathbf{f}[i,j,k]|, \\
D_y(|\mathbf{f}|) &= |\mathbf{f}[i,j+1,k]| - |\mathbf{f}[i,j,k]|, \\
D_z(|\mathbf{f}|) &= |\mathbf{f}[i,j,k+1]| - |\mathbf{f}[i,j,k]|
\end{aligned} \quad (19)
$$

where $\mathbf{f}[i,j,k]$ denotes the reflectivity belonging to the $i, j,$ k^{th} voxel of the imaging scene.

ADMM [13], [14], [16]

1. Set $k = 0$, choose $\mu > 0$, $\mathbf{z}_0$, $\mathbf{d}_0$
2. **repeat**
3. $\mathbf{x}_{k+1} = \underset{\mathbf{f}}{\operatorname{argmin}} \|\mathbf{Af} - \mathbf{y}\|_2^2 + \frac{\mu}{2}\|\mathbf{f} - \mathbf{z}_k - \mathbf{d}_k\|_2^2$
4. $\mathbf{z}_{k+1} = \operatorname{soft}\left(\mathbf{f}_{k+1} + \mathbf{d}_k, \frac{\lambda}{\rho}\right)$
5. $\mathbf{d}_{k+1} = \mathbf{d}_k - \mathbf{f}_{k+1} + \mathbf{z}_{k+1}$
6. $k \leftarrow k + 1$
7. **until** some stopping criterion is satisfied.

C-SALSA-2 [14]

1. Set $k = 0$, choose $\mu > 0$, $\mathbf{z}_0^{(1)}$, $\mathbf{z}_0^{(2)}$, $\mathbf{d}_0^{(1)}$, $\mathbf{d}_0^{(2)}$
2. **repeat**
3. $\mathbf{r}_k = \boldsymbol{\Phi}^H(\mathbf{z}_k^{(1)} + \mathbf{d}_k^{(1)}) + \mathbf{A}^H(\mathbf{z}_k^{(2)} + \mathbf{d}_k^{(2)})$
4. $\mathbf{x}_{k+1} = (\boldsymbol{\Phi}^H\boldsymbol{\Phi} + \mathbf{A}^H\mathbf{A})^{-1}\mathbf{r}_k$
5. $\mathbf{z}_{k+1}^{(1)} = \operatorname{soft}\left(\boldsymbol{\Phi}\mathbf{f}_{k+1} - \mathbf{d}_k^{(1)}, \frac{1}{\mu}\right)$
6. $\mathbf{z}_{k+1}^{(2)} = \mathbf{y} + \begin{cases} \mathbf{Af}_{k+1} - \mathbf{d}_k^{(2)} - \mathbf{y}, & \text{if } \left\|\mathbf{Af}_{k+1} - \mathbf{d}_k^{(2)} - \mathbf{y}\right\|_2 \leq \varepsilon \\ \varepsilon\dfrac{\left(\mathbf{Af}_{k+1} - \mathbf{d}_k^{(2)} - \mathbf{y}\right)}{\left\|\mathbf{Af}_{k+1} - \mathbf{d}_k^{(2)} - \mathbf{y}\right\|_2}, & \text{if } \left\|\mathbf{Af}_{k+1} - \mathbf{d}_k^{(2)} - \mathbf{y}\right\|_2 > \varepsilon \end{cases}$
7. $\mathbf{d}_{k+1}^{(1)} = \mathbf{d}_k^{(1)} - \boldsymbol{\Phi}\mathbf{f}_{k+1} + \mathbf{z}_{k+1}^{(1)}$
8. $\mathbf{d}_{k+1}^{(2)} = \mathbf{d}_k^{(2)} - \mathbf{Af}_{k+1} + \mathbf{z}_{k+1}^{(2)}$
9. $k \leftarrow k + 1$
10. **until** some stopping criterion is satisfied.

V. RECONSTRUCTION ALGORITHMS

We have considered two convex optimization based algorithms for sparse reconstruction, namely, ADMM and C-SALSA-2 and they are explained in the following subsections.

A. ADMM

One approach to solve the problem in (14) is to employ the ADMM whose algorithmic steps are given above. In each iteration of the algorithm, $\mathbf{f}$ and $\mathbf{z}$ vectors are updated in order by applying alternating minimization of augmented Lagrangian.

In a large-scale imaging problem, 3rd step is computationally most demanding part of the algorithm, since it solves a minimization problem. Here we solve this minimization problem iteratively with an inner iteration (e.g. using conjugate gradient least squares (CGLS)), where multiplication of a vector with the sensing matrix $\mathbf{A}$ and its Hermitian $\mathbf{A}^H$ is efficiently carried out through FMM.

In the literature, the optimal value of λ is found by a search method (e.g. cross-validation), which requires solution of (14) multiple times to obtain its best value [40], [42]. This increases the computation time by the number of trials for different λ values. This is another reason to employ the FMM formulation to accelerate the algorithm.

B. C-SALSA-2

In [19], C-SALSA is proposed to solve the constrained sparsity-regularized problem in (15) by adding an indicator function to its objective function, which basically transforms it into an unconstrained problem. Then, resulting problem is transformed into another problem by variable splitting and it is solved by ADMM. The parameter selection is simpler in the constrained problem since (15) does not possess the regularization parameter λ.

The algorithmic steps for C-SALSA-2 are given above. As can be seen, 3rd, 4th, 6th, and 8th steps of C-SALSA-2 involve the product of a vector with the sensing matrix $\mathbf{A}$ and its Hermitian $\mathbf{A}^H$. Here we compute these operations efficiently using FMM as described in Section III. The computationally most demanding step of the algorithm is the 4th step where the inverse of $(\boldsymbol{\Phi}^H\boldsymbol{\Phi} + \mathbf{A}^H\mathbf{A})$ is calculated. This step can be rewritten as a matrix equation in $\mathbf{f}_{k+1}$

$$\left(\boldsymbol{\Phi}^H\boldsymbol{\Phi} + \mathbf{A}^H\mathbf{A}\right)\mathbf{f}_{k+1} = \boldsymbol{\Phi}^H\left(\boldsymbol{\Phi}\mathbf{f}_{k+1}\right) + \mathbf{A}^H\left(\mathbf{Af}_{k+1}\right) = \mathbf{r}_k \quad (20)$$

and since $\mathbf{r}_k$ is known from the 3rd step, the linear system of equations in (20) can be solved iteratively again, enabling to incorporate efficient implementations of multiplications with $\mathbf{A}$ or $\mathbf{A}^H$.

For an imaging problem with an unknown vector of high dimension, solving (20) iteratively is still not feasible by forming the large-scale sensing matrix and computing the necessary matrix-vector products. Here, we accelerate this computation by applying two consecutive FMMs to obtain $\mathbf{A}^H(\mathbf{Af}_{k+1})$, i.e., 1st FMM is for $\mathbf{Af}_{k+1}$ and 2nd FMM is for $\mathbf{A}^H(\mathbf{.})$, which provide a great reduction in computation of 4th step. Furthermore, in practice, the discrete gradient operators (D_x, D_y, and D_z) are also not required to be formed explicitly since they can be computed by filtering the unknown vector with appropriate derivative kernels, e.g. $\begin{bmatrix} -1 & 0 & 1 \end{bmatrix}$, along all directions.

VI. NUMERICAL RESULTS

Several near-field imaging problems are considered to investigate the performance of augmented Lagrangian approach and the related algorithms described above. As sketched in Fig. 3(a), a plus-shaped MIMO array is used in our imaging scenarios, containing equally spaced 30 transmitting antennas and 30 receiving antennas. Aperture of the array is 0.725 m × 0.725 m and spacing between the antennas is 0.025 m. The target is located 0.55 m away from the center of the array (which is assumed to be the nine point scatterers depicted in Fig. 3(b)). Operational frequency
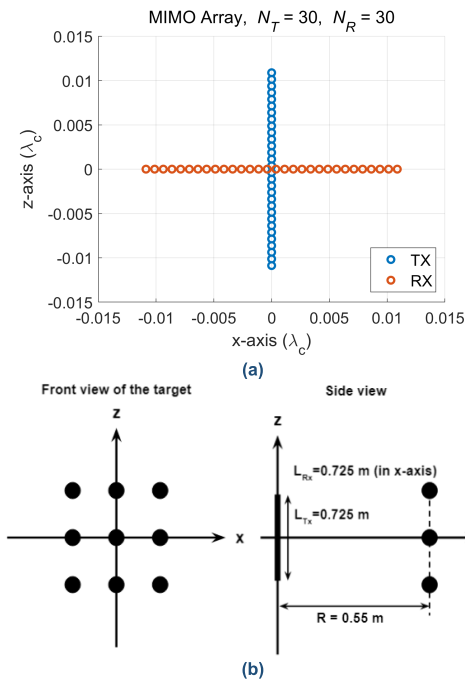
FIGURE 3. (a) Plus-shaped MIMO array, (b) dimensions of the imaging setup.

bandwidth ranges from 7 GHz to 13 GHz with 7 frequency steps of 1 GHz. It must be noted that number of frequency steps are deliberately kept low so that we can analyze how the algorithms and the sparsity constraint perform for under-determined nature of the problems.

For such imaging setup, theoretical cross-range resolution is related to the wavelength at the center frequency λ_c, distance to the target R, and aperture width of the array in orthogonal dimensions. On the other hand, down-range resolution is determined by speed of light and the operational bandwidth. Vertical (along z-axis) and horizontal (along x-axis) cross-range "Rayleigh" resolutions are given by

$$\delta_x = \frac{\lambda_c R}{L_{T,x} + L_{R,x}} \qquad (21)$$

and

$$\delta_z = \frac{\lambda_c R}{L_{T,z} + L_{R,z}}, \qquad (22)$$

respectively. $L_{T,x}$ and $L_{R,x}$ are widths of the transmitting and receiving arrays along x-axis, whereas $L_{T,z}$ and $L_{R,z}$ are widths along z-axis [34]. The down-range "Rayleigh" resolution is given by

$$\delta_y = \frac{c}{2B}. \qquad (23)$$

The down-range resolution of the setup shown in Fig. 4(a) is 0.025 m. The cross-range resolutions calculated by (28) and (22) are equal to 0.025 m and they correspond to the definition of "Rayleigh resolution", which can be written as

Rayleigh Resolution = $k \times$ Null-to-Null Width

$\times$ of Point Spread Function (24)

where the point spread function (PSF) is response of imaging setup to a point scatterer and k is a subjective constant which is typically 0.5 or 1.0. Since the MIMO array has a rectangular aperture, it is selected as 1.0 in this study. Note that this definition is valid for high SNR cases. On the other hand, for very low SNR cases, Cramér-Rao bound must be considered, however, it is not included in this study.

We considered three target scenarios and numerically simulated them in MATLAB using a workstation with Intel(R) Xeon(R) CPU E5-2650 2.60 GHz processor and 128 GB RAM. For comparing the performance of the sparsity-inducing algorithms (ADMM and C-SALSA-2), conventional CGLS is also implemented.

In our simulations, the signal power is defined as

$$S = N_T N_R N_F \left(\frac{1}{N_V} \sum_{\substack{q=1 \\ f_q \neq 0}}^{N_V} \frac{f_q}{R_{T_m,q}^2 R_{R_n,q}^2} \right) \qquad (25)$$

where the term in the parenthesis is the average return power from the image scene. The total power is given by $N_T N_R N_F$ times this quantity, because we are using N_T transmitters, N_R receivers, and N_F frequency steps. Note that this definition strongly depends on the shape and reflectivity distribution of the target, since averaging is done over non-empty voxels.

Quality of the results are estimated with respect to peak signal-to-noise ratio (pSNR) of reconstructed reflectivity images, defined by

$$\text{pSNR} = 10\log_{10}\left(\frac{\text{MAX}_I^2}{\text{MSE}} \right) \qquad (26)$$

where, MAX_I is maximum voxel value of reconstructed reflectivity image and MSE is mean squared error which can be simply defined as the mean of the square of the difference between the noise-free $m \times n$ reference image I and $\hat{I}$, which is the image reconstructed from the noisy measurement as

$$\text{MSE} = \frac{1}{mn} \sum_{i=1}^{m} \sum_{j=1}^{n} \left[I(i,j) - \hat{I}(i,j) \right]^2. \qquad (27)$$

Note that all simulations given below are carried out with 30 dB input SNR.

A. POINT SCATTERERS

In the first scenario, the scene contains an array of 9 point scatterers located on a grid of 0.025 m on each side on the $y = 0.55$ m plane. The reflectivity level of the point scatterer at the center is set to 0.5, whereas all other scatterers have a reflectivity of 1. Fig. 4(a) shows actual reflectivities of the scatterers for this scenario. The images are reconstructed by solving (14) using the developed efficient ADMM approach with FMM. Here $\|\mathbf{f}\|_1$ is used as regularization function. Note that this problem can also be solved by the developed C-SALSA-2 approach with the same regularization function, however, we preferred using ADMM in order to demonstrate
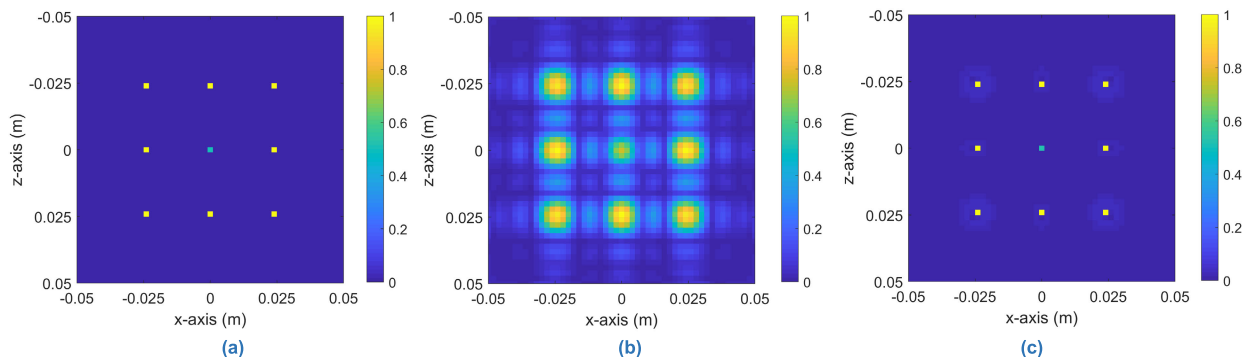
FIGURE 4. Imaging results for the first scenario: (a) Actual reflectivity of the point scatterers, (b) CGLS reconstruction, and (c) sparsity-based reconstruction by ADMM. The reconstructions are realized with the developed FMM-based approaches and normalized by the largest value, therefore, they share the same colorbar.
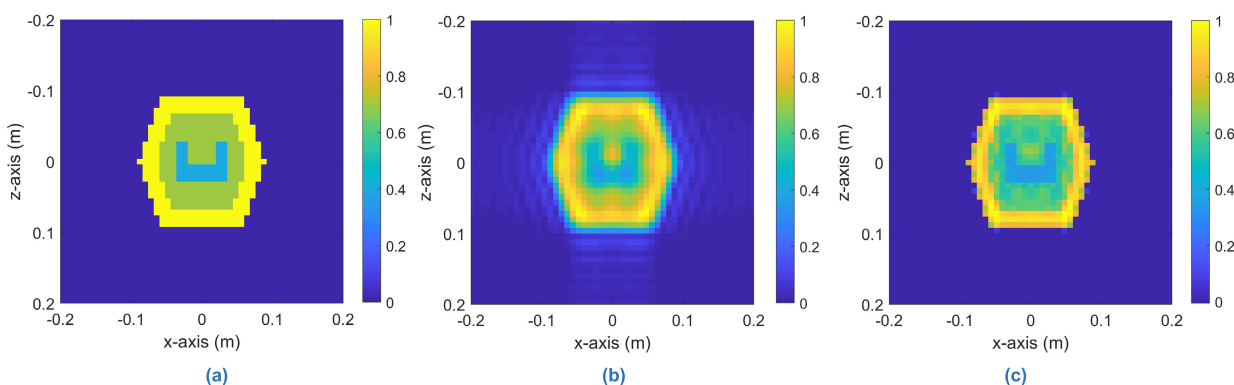

FIGURE 5. Imaging results for the hexagon-shaped target: (a) Actual reflectivity of the hexagonal target, (b) CGLS reconstruction, and (c) sparsity-based reconstruction by C-SALSA-2. The reconstructions are realized with the developed FMM-based approaches and normalized by the largest value, therefore, they share the same colorbar.

applicability of FMM in different sparse reconstruction algorithms. The images are formed on $y = 0.55$ m plane with a resolution of 2 mm in both directions, resulting in a total of 2601 pixels. The reconstructions are normalized by the largest value and corresponding images obtained by CGLS and ADMM are given in Fig. 4(b) and Fig. 4(c), respectively.

The results show that the theoretical cross range "Rayleigh" resolutions can be achieved by solving the problem with ADMM. On the other hand, CGLS cannot provide a focused image under the same conditions, which emphasize the superior focusing performance of sparsity-based reconstruction. The relative reflectivity levels of the point scatterers in the image reconstructed by ADMM are closer to the actual values as compared to the results of CGLS.

The quality of the reconstructed images is quantitatively evaluated by calculating their pSNRs, which are 12.36 dB and 42.17 dB for CGLS and ADMM, respectively. In computational image formation, pSNR lower than 20 dB is accepted to be low-quality while pSNR higher than 40 dB is considered to be almost excellent quality [39]. Hence, the calculated pSNRs and difference between them indicate that ADMM performs more effectively for the reconstruction of a sparse scene compared to the conventional CGLS.

B. EXTENDED TARGETS
For the reconstruction of extended targets, two different cases are considered: (i) a 2-D hexagonal target and (ii) 3-D concentric cylinders. The developed efficient C-SALSA-2 algorithm with FMM is used to reconstruct the images that are given in this subsection. TV of the magnitude is used as the regularization function.

1) HEXAGONAL TARGET
The actual reflectivity of the hexagonal target is illustrated in Fig. 5(a). The target is a planar structure of size 0.4 m × 0.4 m located at $y = 0.55$ m plane, and the image is constructed using 4 mm by 4 mm pixels, which makes 10201 pixels in total. Reflectivity level distribution of the target is non-uniform, i.e., reflectivity of the outer part is 1, whereas it is 0.6 for the inner parts except for the U-shaped section, which has a reflectivity of 0.4. The measurements are simulated using the discrete model given in (7) and the reflectivity images are reconstructed by CGLS and C-SALSA-2. Fig. 5(b) and Fig. 5(c) respectively shows the normalized reconstructions obtained by CGLS and C-SALSA-2, where the color scale shows the magnitude of the reflectivity distribution of the imaging scene along x- and z-directions.
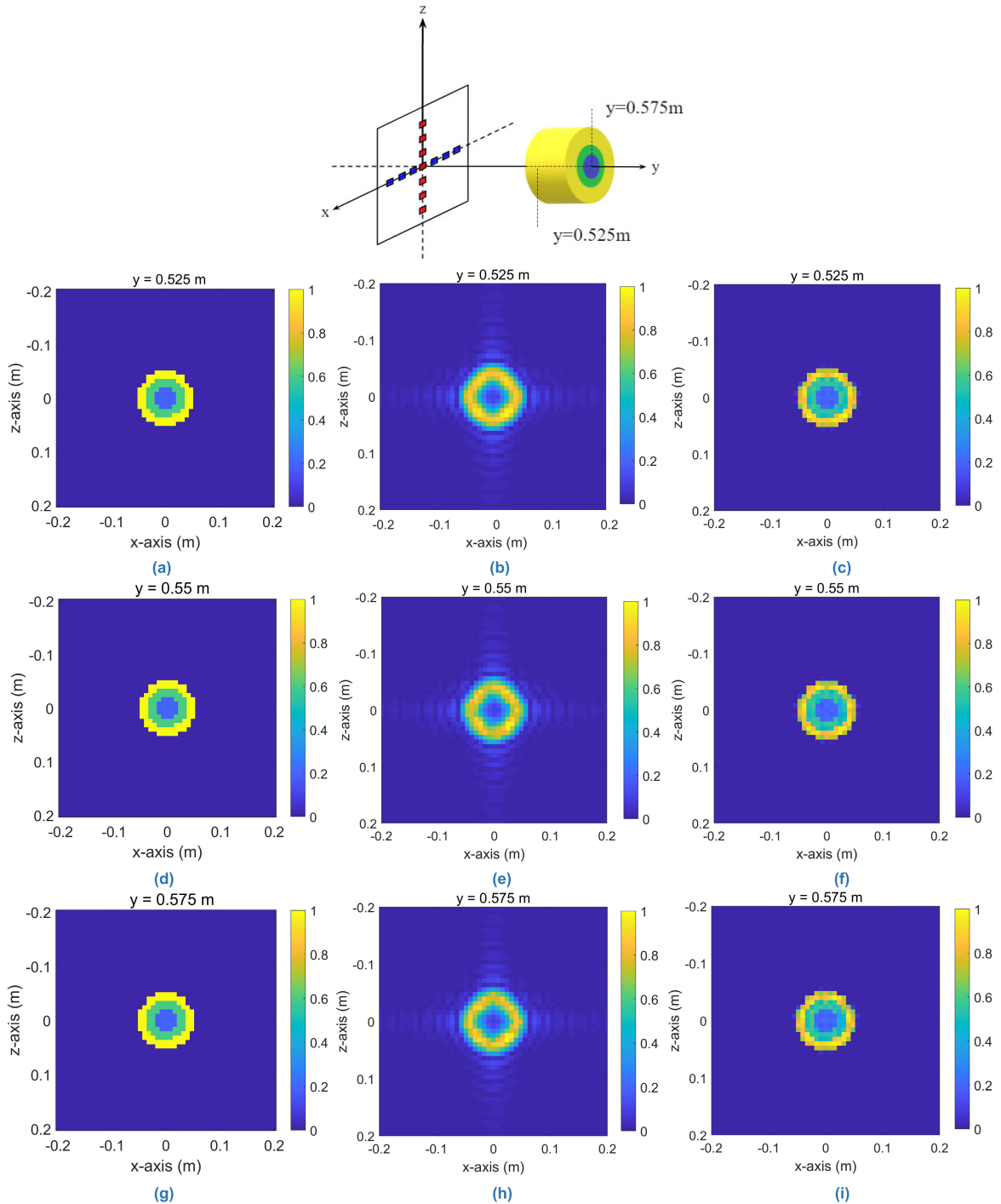
FIGURE 6. Imaging results for the concentric cylinders. The left, the middle and the right columns sketch actual reflectivity of the cylinders, CGLS reconstruction and sparsity-based reconstruction with C-SALSA-2, respectively. All reconstructions are realized with the developed FMM-based approaches normalized by the largest value, therefore, they share the same colorbar. The first, the second, and the third rows shows the images, belonging to the $y = 0.525$ m, $y = 0.55$ m, and $y = 0.575$ m slices, respectively.

The results demonstrate that the characteristics of the hexagonal target such as the edges where the reflectivity rapidly changes and the U-shaped section is blurry, when the image is reconstructed using CGLS. On the other hand, solving with C-SALSA-2 provides a well-focused image, containing all details of the target.

Furthermore, the background that does not contain any scatterer is clearer in the reconstructed image obtained by C-SALSA-2. The pSNR values for CGLS and C-SALSA-2 are calculated as 22.95 dB and 36.23 dB, respectively, which mathematically support our observations. For one matrix-vector product, efficient computation time

is measured as ~54.9 seconds, while memory usage is ~1.07 GBytes.

2) CONCENTRIC CYLINDERS

In the last scenario, we considered a 3-D object that is formed by three concentric cylinders, lying along the range direction between $y = 0.525$ m and $y = 0.575$ m planes. Left column of Fig. 6 provides the actual reflectivity of the cylinders at three different cross-sections on $y = 0.525$ m, $y = 0.55$ m, and $y = 0.575$ m planes. The radii of the cylinders are, from outer to inner, 6 cm, 4 cm, and 2 cm, respectively, and corresponding reflectivities are 1, 0.6, and 0.2. The imaging volume is roughly digitized such that it is confined to a volume of 0.4 m × 0.4 m × 0.25 m with voxel size of 8 mm × 8 mm × 2.5 mm, giving 28611 voxels in total. The reflectivity distribution of the imaging volume is reconstructed by applying CGLS and C-SALSA-2 on (7) and the resulting images of the 3-D object are provided by 2-D images for the corresponding cross-sections. The normalized reflectivity images obtained by CGLS and C-SALSA-2 are depicted in the middle and right columns of Fig. 6, respectively.

The slices in Fig. 6(b), Fig. 6(e), and Fig. 6(h) show that it is not possible to attain well-focused reconstruction by CGLS e.g., the concentric cylinders are blurry and reflectivity changes are not exactly how they should be. Conversely, as can be clearly seen in Fig. 6(c), Fig. 6(f), and Fig. 6(i), the reconstructions by C-SALSA-2 results visibly more accurate images in terms of reflectivity distribution and contrast transitions between the cylinders. Besides, the calculated pSNRs for CGLS and C-SALSA-2 reconstructions are 22.87 dB and 36.50 dB, respectively, which support our observations. Besides, efficient computation time and memory requirement per matrix-vector product respectively take ~162.7 seconds and 3.1 GBytes.

We further investigate the performance of FMM-based sparse reconstruction method for different input SNR values. To do this, we repeated the simulations of the concentric cylinders with C-SALSA-2 and CGLS, each time decreasing the input SNR gradually from 50 dB to 0 dB and measuring the pSNR values of the reconstructed reflectivity images. Fig. 7 plots the pSNRs as a function of input SNR value for both C-SALSA-2 and CGLS. As can be seen, C-SALSA-2 can still provide pSNR above 20 dB although the input SNR is about 5 dB. On the other hand, conventional CGLS cannot handle noise presence as well as C-SALSA-2 due to the lack of regularization term and its pSNR continuously decreases after the input SNR gets lower than 25 dB. Fig. 8 shows the reconstructions obtained by CGLS and C-SALSA-2 for the hexagonal target when different input SNR values are applied.

Finally, we analyzed the computational performance of FMM. As stated earlier, the sparsity-based reconstruction algorithms require solving multiple forward problems at each iteration. Direct computation of the forward problems with N unknowns leads to immense computational burden for
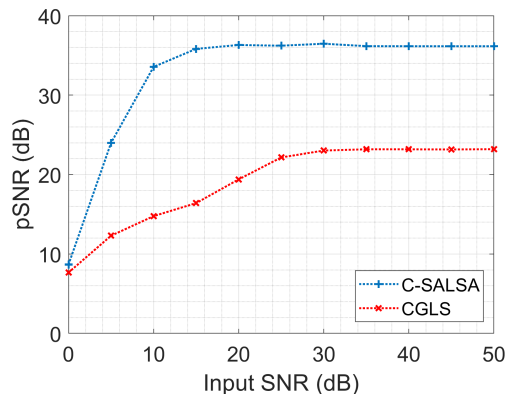

FIGURE 7. Performance of FMM-applied sparsity-based reconstruction with C-SALSA-2 and CGLS for the concentric cylinders under different input SNRs.
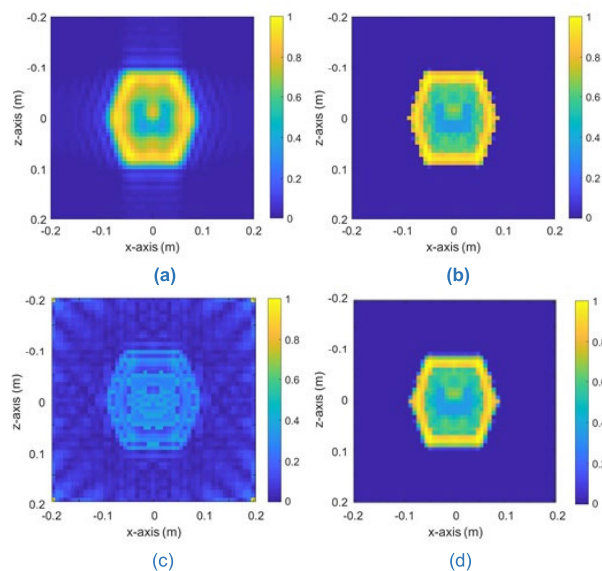

FIGURE 8. Reconstructions obtained by CGLS and C-SALSA-2 for different input SNR values. (a) CGLS reconstruction for 30 dB input SNR (pSNR = 23.36 dB). (b) C-SALSA-2 reconstruction for 30 dB input SNR (pSNR = 36.15 dB). (c) CGLS reconstruction for 10 dB input SNR (pSNR = 8.12 dB). (d) C-SALSA-2 reconstruction for 10 dB input SNR (pSNR = 33.42 dB). All reconstructions are realized with the developed FMM-based approaches and normalized by the largest value, therefore, they share the same colorbar.

large imaging problems due to the per-iteration complexity of $O(N^2)$. On the other hand, FMM calculates the matrix-vector product in a group-by-group manner (see Section III for our grouping method), hence, reduces the computational complexity to $O(N^{3/2})$ for both processing time and memory at each iteration.

The efficiency of FMM is also demonstrated by simulating the same target scenario with different number of antennas. Fig. 9 plots processing time (in seconds) and memory requirement (in Mbytes) as a function of total number of antennas (i.e., $N_T = N_R$). As proposed, FMM outperforms the direct matrix-vector product above a specific number of antennas,
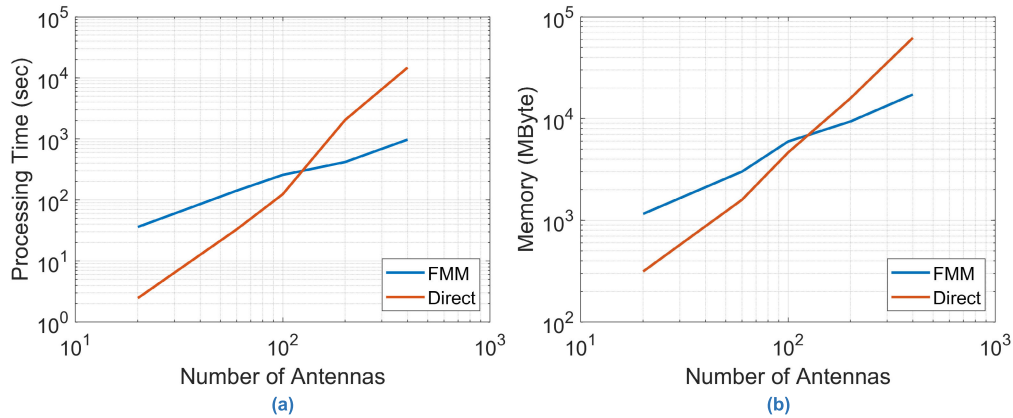
FIGURE 9. Comparison of the FMM and direct matrix-vector product in terms of (a) processing time and (b) memory.

which we call crossover point, in terms of processing time and memory. Note that this crossover point depends on several things that must be considered, i.e., type of application, how the forward (sensing) operator is implemented, truncation order of the FMM, etc.

VII. CONCLUSION

In this paper, we solve near-field imaging problems and seek sparse solution for them. A MIMO radar configuration is considered for the imaging and corresponding forward problem is implemented using Born approximation. Then, the problem is discretized and turned into a linear system of equations, the structure of which is exploited to apply a two stage FMM, thus, large-scale problems can be solved in an efficient way. The problems are solved by two sparsity-inducing algorithms (ADMM and C-SALSA-2) in conjunction with appropriate regularization functions (ℓ_1-norm and *TV*) according to the properties of the imaged scene and reflectivity characteristics of the targets. We validated our approach by a series of numerical tests conducted in comparison with a classical solver. Results demonstrate that well-focused images can be constructed for different type of near-field imaging scenarios, ranging from point scatterers to 3-D continuous targets, despite low input SNR. When FMM is applied to the solution of the problem, quality of the reconstructions can still be preserved. Furthermore, as the dimensions of the problem increases, which is number of antennas in our case, FMM makes the solution very efficient in terms of processing time and memory requirement.

REFERENCES

[1] F. Fioranelli, S. Salous, and X. Raimundo, "Frequency-modulated interrupted continuous wave as wall removal technique in through-the-wall imaging," *IEEE Trans. Geosci. Remote Sens.*, vol. 52, no. 10, pp. 6272–6283, Oct. 2014.

[2] A. Beeri and R. Daisy, "High-resolution through-wall imaging," *Proc. SPIE*, vol. 6201, May 2006, Art. no. 62010J.

[3] A. G. Yarovoy, T. G. Savelyev, P. J. Aubry, P. E. Lys, and L. P. Ligthart, "UWB array-based sensor for near-field imaging," *IEEE Trans. Microw. Theory Techn.*, vol. 55, no. 6, pp. 1288–1295, Jun. 2007.

[4] M. Klemm, J. A. Leendertz, D. Gibbins, I. J. Craddock, A. Preece, and R. Benjamin, "Microwave radar-based differential breast cancer imaging: Imaging in homogeneous breast phantoms and low contrast scenarios," *IEEE Trans. Antennas Propag.*, vol. 58, no. 7, pp. 2337–2344, Jul. 2010.

[5] X. Zhuge and A. Yarovoy, "Near-field ultra-wideband imaging with two-dimensional sparse MIMO array," in *Proc. 4th Eur. Conf. Antennas Propag.*, Barcelona, Spain, 2010, pp. 1–4.

[6] S. S. Ahmed, A. Schiess, and L. Schmidt, "Near field mm-wave imaging with multistatic sparse 2D-arrays," in *Proc. Eur. Radar Conf. (EuRAD)*, Rome, Italy, 2009, pp. 180–183.

[7] J. A. Tropp and S. J. Wright, "Computational methods for sparse solution of linear inverse problems," *Proc. IEEE*, vol. 98, no. 6, pp. 948–958, Apr. 2010.

[8] W. Tan, P. Huang, Z. Huang, Y. Qi, and W. Wang, "Three-dimensional microwave imaging for concealed weapon detection using range stacking technique," *Int. J. Antennas Propag.*, vol. 2017, pp. 1–11, Aug. 2017.

[9] S. Li, G. Zhao, H. Li, B. Ren, W. Hu, Y. Liu, W. Yu, and H. Sun, "Near-field radar imaging via compressive sensing," *IEEE Trans. Antennas Propag.*, vol. 63, no. 2, pp. 828–833, Feb. 2015.

[10] Y. Alvarez, Y. Rodriguez-Vaqueiro, B. Gonzalez-Valdes, C. Rappaport, F. Las-Heras, and J. Martinez-Lorenzo, "Three-dimensional compressed sensing-based millimeter-wave imaging," *IEEE Trans. Antennas Propag.*, vol. 63, no. 12, pp. 5868–5873, Dec. 2015.

[11] L. Ding, Y. Ye, G. Ye, X. Wang, and Y. Zhu, "Bistatic synthetic aperture radar with undersampling for terahertz 2-D near-field imaging," *IEEE Trans. THz Sci. Technol.*, vol. 8, no. 2, pp. 174–182, Mar. 2018.

[12] S. S. Chen, D. L. Donoho, and M. A. Saunders, "Atomic decomposition by basis pursuit," *SIAM Rev.*, vol. 43, no. 1, pp. 129–159, 2001.

[13] G. Davis, S. Mallat, and M. Avellaneda, "Adaptive greedy approximations," *Constructive Approx.*, vol. 13, no. 1, pp. 57–98, 1997.

[14] A. C. Gilbert, M. Muthukrsihnan, and M. J. Strauss, "Approximation of functions over redundant dictionaries using coherence," in *Proc. 14th Annu. ACM-SIAM Symp. Discrete Algorithms*, Jan. 2003, pp. 243–252.

[15] D. L. Donoho, Y. Tsaig, I. Drori, and J.-L. Starck, "Sparse solution of underdetermined linear equations by stagewise orthogonal matching pursuit," *IEEE Trans. Inf. Theory*, vol. 58, no. 2, pp. 1094–1121, Feb. 2012.

[16] A. M. Bruckstein, D. L. Donoho, and M. Elad, "From sparse solutions of systems of equations to sparse modeling of signals and images," *SIAM Rev.*, vol. 51, no. 1, pp. 34–81, Feb. 2009.

[17] H. Güven, A. Güngör, and M. Çetin, "An augmented Lagrangian method for complex-valued compressed SAR imaging," *IEEE Trans. Comput. Imag.*, vol. 2, no. 3, pp. 235–250, Sep. 2016.

[18] M. V. Afonso, J. M. Bioucas-Dias, and M. A. T. Figueiredo, "An augmented Lagrangian approach to the constrained optimization formulation of imaging inverse problems," *IEEE Trans. Image Process.*, vol. 20, no. 3, pp. 681–695, Mar. 2011.

[19] S. J. Wright, R. D. Nowak, and M. A. T. Figueiredo, "Sparse reconstruction by separable approximation," *IEEE Trans. Signal Process.*, vol. 57, no. 7, pp. 2479–2493, Jul. 2009.

[20] M. V. Afonso, J. M. Bioucas-Dias, and M. A. T. Figueiredo, "Fast image recovery using variable splitting and constrained optimization," *IEEE Trans. Image Process.*, vol. 19, no. 9, pp. 2345–2356, Sep. 2010.

[21] M. A. T. Figueiredo, J. M. Bioucas-Dias, and M. V. Afonso, "Fast frame-based image deconvolution using variable splitting and constrained optimization," in *Proc. IEEE/SP 15th Workshop Stat. Signal Process.*, Cardiff, U.K., Aug. 2009, pp. 109–112.

[22] A. N. Tikhonov and V. Y. Arsenin, *Solution of Ill-Posed Problems*. Washington, DC, USA: Winston & Sons, 1977.

[23] S. Gazzola and J. G. Nagy, "Generalized arnoldi-tikhonov method for sparse reconstruction," *SIAM J. Sci. Comput.*, vol. 36, no. 2, pp. B225–B247, Jan. 2014.

[24] S. Liu, H. Wu, Y. Huang, Y. Yang, and J. Jia, "Accelerated structure-aware sparse Bayesian learning for three-dimensional electrical impedance tomography," *IEEE Trans. Ind. Informat.*, vol. 15, no. 9, pp. 5033–5041, Sep. 2019.

[25] N. Antipa, G. Kuo, R. Heckel, B. Mildenhall, E. Bostan, R. Ng, and L. Waller, "DiffuserCam: Lensless single-exposure 3D imaging," *Optica*, vol. 5, no. 1, pp. 1–9, 2018.

[26] O. F. Kar and F. S. Oktem, "Compressive spectral imaging with diffractive lenses," *Opt. Lett.*, vol. 44, no. 18, pp. 4582–4585, 2019.

[27] D. Bi, X. Li, X. Xie, Y. Xie, and Y. R. Zheng, "Compressive sensing operator design and optimization for wideband 3-D millimeter-wave imaging," *IEEE Trans. Microw. Theory Techn.*, early access, Aug. 9, 2021, doi: 10.1109/TMTT.2021.3100499.

[28] S. Li, G. Zhao, H. Sun, and M. Amin, "Compressive sensing imaging of 3-D object by a holographic algorithm," *IEEE Trans. Antennas Propag.*, vol. 66, no. 12, pp. 7295–7304, Dec. 2018.

[29] R. Coifman, V. Rokhlin, and S. Wandzura, "The fast multipole method for the wave equation: A pedestrian prescription," *IEEE Antennas Propag. Mag.*, vol. 35, no. 3, pp. 7–12, Jun. 1993.

[30] C.-C. Lu and W. C. Chew, "A multilevel algorithm for solving a boundary integral equation of wave scattering," *Microw. Opt. Technol. Lett.*, vol. 7, no. 10, pp. 466–470, Jul. 1994.

[31] J. M. Song and W. C. Chew, "Multilevel fast multipole algorithm for solving combined field integral equations of electromagnetic scattering," *Microw. Opt. Tech. Lett.*, vol. 10, pp. 14–19, Sep. 1995.

[32] E. A. Miran and S. Koc, "The fast multipole method for sparse solution of linear inverse scattering problems," in *Proc. 18th Medit. Microw. Symp. (MMS)*, Oct. 2018, pp. 407–410.

[33] X. Zhuge and A. Yarovoy, "Near-field ultra-wideband imaging with two-dimensional sparse MIMO array," in *Proc. 4th EuCAP*, Apr. 2010, pp. 1–4.

[34] X. Zhuge and A. G. Yarovoy, "A sparse aperture MIMO-SAR-based UWB imaging system for concealed weapon detection," *IEEE Trans. Geosci. Remote Sens.*, vol. 49, no. 1, pp. 509–518, Jan. 2011.

[35] P. M. Morse and H. Feshbach, *Method of Theoretical Physics*. New York, NY, USA: McGraw-Hill, 1953.

[36] X. Zhuge and A. G. Yarovoy, "Three-dimensional near-field MIMO array imaging using range migration techniques," *IEEE Trans. Image Process.*, vol. 21, no. 6, pp. 3026–3033, Jun. 2012.

[37] S. Koc, J. Song, and W. C. Chew, "Error analysis for the numerical evaluation of the diagonal forms of the scalar spherical addition theorem," *SIAM J. Numer. Anal.*, vol. 36, no. 3, pp. 906–921, Jan. 1999.

[38] J. Song and W. C. Chew, "Error analysis for the truncation of multipole expansion of vector Green's functions," *IEEE Microw. Compon. Lett.*, vol. 11, no. 7, pp. 311–313, Jul. 2001.

[39] F. S. Oktem, "Sparsity-based three-dimensional image reconstruction for near-field MIMO radar imaging," *TURKISH J. Electr. Eng. Comput. Sci.*, vol. 27, no. 5, pp. 3282–3295, Sep. 2019.

[40] G. H. Golub, M. Heath, and G. Wahba, "Generalized cross-validation as a method for choosing a good ridge parameter," *Technometrics*, vol. 21, no. 2, pp. 215–223, May 1979.

EMRE A. MIRAN received the B.S. degree in electrical and electronics engineering from Dokuz Eylul University, Izmir, Turkey, in 2012. He is currently pursuing the Ph.D. degree with the Electrical and Electronics Engineering Department, Middle East Technical University, Ankara, Turkey. From 2012 to 2017, he was a Teaching/Research Assistant with the Electrical and Electronics Engineering Department, Middle East Technical University. Since 2017, he has been a Researcher with the Microwave and Millimeter-Wave Research Laboratory, Electrical and Electronics Engineering Department. At the same time, he is working as RF/Antenna Design Engineer at Engitek Ltd., Company. His research interests include electromagnetics, antenna design, RF system design, and radar imaging.

FIGEN S. OKTEM (Member, IEEE) received the B.S. and M.S. degrees in electrical and electronics engineering from Bilkent University, Ankara, Turkey, in 2007 and 2009, respectively, and the Ph.D. degree in electrical and computer engineering from the University of Illinois at Urbana–Champaign (UIUC), Champaign, IL, USA, in 2014. She is currently an Associate Professor with the Electrical and Electronics Engineering Department, Middle East Technical University (METU), Ankara. Before joining METU, she was a Postdoctoral Research Associate with the NASA Goddard Space Flight Center, where she worked on the development of high-resolution spectral imaging techniques. Her research interests include statistical signal processing, optical information processing, computational imaging, and inverse problems. Her main research interests include development of novel computational imaging and sensing technologies and their applications in physical and life sciences. She is a member of OSA. She was a recipient of the Professor Kung Chie Yeh Endowed Fellowship from the Department of Electrical and Computer Engineering, UIUC, in 2012, and the NASA Earth and Space Science Fellowship, from 2012 to 2014.

SENCER KOC received the B.S., M.S., and Ph.D. degrees in electrical engineering from Middle East Technical University, Ankara, Turkey, in 1979, 1983, and 1987, respectively. He is currently a Full Professor with the Department of Electrical and Electronics Engineering, Middle East Technical University. His research interests include numerical methods in electromagnetic theory, antenna measurements, and RF MEMS devices.

• • •